RSC Advances

ROYAL SOCIETY OF CHEMISTRY

www.rsc.org/advances

Segmental dynamics, morphology and thermomechanical properties of electrospun poly(ε-caprolactone) nanofibers in presence of an interacting filler

Eldho Elias,[1,2] Sarath Chandran C,[1,2] Nithin Chandran,[1,2] Fernando G. Souza Jr,[3] and Sabu Thomas[1,2]

[1] School of Chemical Science, Mahatma Gandhi University, P.D Hills P.O, Kottayam, Kerala, 686560, India.

[2] International and Inter University Center for Nanoscience and Nanotechnology, Mahatma Gandhi University, P.D Hills, Kottayam, Kerala, 686560, India.

[3] Programa de Engenharia Civil, COPPE, Centro de Tecnologia - Cidade Universitária, av. Horacio Macedo, 2030, bloco I. Universidade Federal de Rio de Janeiro, Brasil.

1. Introduction

Electrospun nanofibers find extensive applications in various fields such as energy and electricity, media filter and sensors, tissue engineering and composite reinforcement. Now-a-days, the studies on the electrospinning process are done extensively.[1–3] However, most of these applications need improved mechanical and thermal properties. In order to modify and improve of these properties, the methods such as blending polymers with each other and the introduction of inorganic fillers into polymer matrix are used.[4–6] Among these methods, inorganic nanofiller reinforced organic polymer nanocomposite fibers are very important mainly due to their nanometer size, high specific surface area, and the associated predominance of interfaces, easy dispersion in polymer matrix and the high thermal stability.[7–9] Various composite nanofibers can exhibit, therefore, novel properties, which are very useful for aerospace, biomedical, defense and energy, and other engineering applications due to enhanced thermal and mechanical properties.[10] It has been observed that the incorporation of clay nanolayers increases the dimensional stability, thermal properties, and mechanical resistance of the polymer matrix compared with other fillers due to their layered

structures.[10] Most polymer nanofibers exhibit these improvements in performance at relatively low loadings (typically less than 5.0 wt%). It has also been found that the conductivities of the polymer/clay solutions increased with raising the content of clay, which caused a decrease in the mean diameter of the polymer clay nanofibers.[11,12] Nanocomposite fibers electrospun from polymer-clay dispersions exhibit enhanced mechanical properties, such as shear modulus, and higher thermal properties, such as glass transition temperature. Polycaprolactone, a synthetic biopolymer with an appropriate biodegradation rate has found to be useful in various biomedical applications. In fact, (PCL) is a semi-crystalline aliphatic polyester with a high degree of crystallinity and hydrophobicity. However pristine PCL has poor mechanical properties, and the hydrophobic nature limits its use as a scaffold material for tissue engineering applications. Incorporation of clay platelets into PCL will be very effective in increasing both shear viscosity and extensional viscosity of the nanocomposite, where the interaction between PCL and clay has a significant role. It would be a good strategy to make these composites and check their possibility as a strong candidate for biomedical applications such as wound healing, water purification and tissue engineering applications. In the present paper, we have carefully evaluated the effect of addition of clay on the segmental dynamics, morphology, mechanical properties and thermal characteristics of electrospun PCL fiber. Even though a plethora of work are available in PCL-clay (Cloisite 15A, Cloisite 20A, Cloisite 30A etc) very few works have been reported using Cloisite 10A, and a detailed investigation of this nanocomposite is very demanding considering their potential use as scaffolds for wound healing and tissue engineering applications.

1. Materials and Methods

Polycaprolactone (M_n= 80000) was obtained from Aldrich and dichloromethane from FlukaChemie. The organically modified montmorillonite clays (Cloisite 10A) were purchased

from southern clay products, India. Figure 1 shows the structural details of Cloisite 10A used for this study.

1.1.Preparation of PCL/ Clay nanocomposite membrane by Electrospinning

In the first step, PCL solution was prepared by dissolving PCL granules in dichloromethane by means of a magnetic stirrer for 24 hours. Nanoclay dispersion was prepared in dichloromethane by using a magnetic stirrer for 36 hours. PCL-Closite 10A nanocomposite slurry was prepared by mixing PCL solution along with nanoclay dispersion with the help of a water bath sonicator. After that the nanocomposite solution was introduced into the electrospinning set up. The electrospinning consists of a syringe pump for the injection of the polymer solution, a metallic collector and a high voltage supply. All experiments were performed using a disposable plastic syringe of 10 ml internal volume and 21G needle diameter. The needle was connected to a high voltage supply (Gamma High voltage research, USA) and the ground electrode was connected to an aluminum foil which served as the ground electrode. TCD distance (The distance between the needle and collector) was kept at 15 cm and the applied voltage was ranged between 7.5 kV and 20 kV. The feed rate of polymer solution was adjusted as 1 ml/hr. Nanocomposites containing 1, 2.5, 5, and 7.5 wt% of clay (Cloisite 10A) were prepared and subjected to detailed investigation.

2. Characterization

2.1 Differential scanning calorimetry (DSC)

Dynamic DSC measurements were performed in a Perkin Elmer Diamond DSC from -80 to +80 °C at a heating rate of 10 °C·min^{-1} with nitrogen as purge gas (ASTM – 3417-83). Endothermic deviations from the baseline during the second heating cycle was used for study.

2.2. Wide angle X-ray scattering (WAXS) analysis

Neat PCL, Cloisite 10A and the nanocomposites were analyzed by WAXS. X–ray diffractograms were recorded by Bruker AXS Automated XRD model D8 equipment having

CuKα1 radiation (λ= 0.154 nm), between a 2θ range from 1° to 75°. The voltage used was 45KV, and the ampere was 30mA.

2.3. Contact angle studies

Contact angle measurements were carried out in a SEO Phoenix instrument. Measurements were carried out with water (triply distilled) on samples of size 1×1×2 cm^3 at room temperature. The volume of the sessile drop was maintained as 5 µl in all cases using a micro syringe. The contact angle was measured within 45–60 s of the addition of the liquid drop with an accuracy of ±1°. Measurements were repeated six to ten times with different test pieces of the same sample to check the accuracy. Also contact angles were measured with definite time intervals for a single drop and the measurements were recorded as snap shots.

2.4. Transmission electron microscopy (TEM)

The dispersion of nanofillers in polymer nanocomposites was investigated using TEM. The micrographs of the nanocomposites were taken in JEOL JEM transmission electron microscope with an accelerating voltage of 200 keV. Here one single fibre was separated from the electrospun mat and used for the analysis.

2.5 Scanning Electron Microscopy (SEM)

JEOL JSM -6390 SEM instrument was employed to observe the microstructures of the material. Fiber morphology as well as the average fiber diameter of the electrospun fibers were analyzed by this technique. The samples were analyzed using an accelerating voltage of 15KV, and the electrospun mat was sputtered with gold.

2.6 Fourier transform infra-red (FT-IR) spectroscopy

FTIR analysis was carried out using attenuated total reflection (ATR) using Perkin-Elmer Spectrum One spectrometer (Lantrisant, UK). FTIR spectra were recorded in transmittance mode over the range of 4000 – 600 cm^{-1} by an averaging 16 scans at a resolution of 4 cm^{-1} in all cases.

2.7 Mechanical properties (UTM)

Mechanical properties of the produced films were studied in the tensile loading condition using UTM (Tinius Olsen HKT 50). Mechanical tests were carried out on rectangular specimens, gauge width 10 mm and gauge length 30 mm. Mechanical tests were performed at 20mm/min to rupture by an electro mechanical machine equipped with a 5 kg load cell. Four specimens were considered for each experiment.

2.8 Thermogravimetric (TG) analysis

TGA measurements were carried out by using Schimadzu TGA instrument. The samples heated from 25 to 700 °C at a hating rate of 10 °C /min under nitrogen. The clay content was measured from the residue left at 410 °C.

2.9 Determination of the in-vitro cytotoxic effect of PCL-Cloisite 10A on cultured L929 cell lines

L929 fibroblast cell lines were purchased from NCCS Pune and these were maintained in Dulbecco's modified eagles media (HIMEDIA) supplemented with 10% FBS (Invitrogen). The cells were grown to confluency at 37°c in 5 % CO2 (NBS, EPPENDORF, GERMANY) in a humidified atmosphere in a CO2 incubator. The cells were further trypsinized (500µl of 0.025% Trypsin in PBS/ 0.5mM EDTA solution (Himedia)) for 2 minutes and passaged to T flasks in complete aseptic conditions. 1µl, 5µl, 10µl, 20µl of both the samples were added and incubated for 24 hours. The % difference in viability was determined by standard MTT assay after 24 hours of incubation. The morphological characteristics of cells were imaged using inverted phase contrast microscope (Olympus CKX41) with Optika Pro5 CCD camera. MTT is a colorimetric assay that measures the reduction of yellow 3-(4, 5dimethythiazol-2-yl)-2, 5-diphenyl tetrazolium bromide (MTT) by mitochondrial succinate dehydrogenase.[13–15] The MTT enters the cells and passes into the mitochondria where it is reduced to an insoluble, coloured (dark purple) formazan product. The cells are then solubilised with an

organic solvent dimethyl sulfoxide (Himedia) and the released, solubilised formazan product was measured at 540nm. Since reduction of MTT can only occur in metabolically active cells the level of activity is a measure of the viability of the cells.The wells containing polymer and cells were washed with 1x PBS and then added 50 µl of MTT solution to the culture (MTT -5mg/ml dissolved in PBS). It was then incubated at 37 °C for 3 hours. MTT was removed by washing with 1x PBS and the formazan was eluted out with 200 µl of Isopropanol. Incubation was done at room temperature for 30 minutes until the cell got lysed and colour was obtained. The solution was transferred to centrifuge tubes and centrifuged at top speed for 2minutes to precipitate cell debris. Optical density was read at 540 nm using DMSO as blank using microplate reader (LISASCAN, Erba).

3. Results and Discussion

The dynamic heterogeneity associated with T_g was first correlated to the extent of cooperatively rearranging regions (CRR) by Adam and Gibbs.[16] Later Doth derived a formula based on the Von laue approach and according to this,[17–20]

$$\xi = \frac{1/\Delta C_p}{\rho\left(\Delta T_g\right)^2} . k_B T_g^2 \qquad (1)$$

$$V_a = \xi^3 \qquad (2)$$

Here ΔC_p is the change in heat capacity between the onset and endset of T_g, k_B the Boltzmann constant, while ΔT_g is the difference between the onset and endset of T_g, ρ is the density (the density of neat PCL and Cloisite 10A was taken as 1.15 and 1.90 $g \cdot cm^{-3}$). Figure 2 shows the calculated values of CRR. It was observed that the CRR values increase as the amount of Cloisite 10A increases indicating improved interaction between the two. As the loading of clay increased to 7.5% a decrease in CRR is observed which can be due to agglomeration of clay causing a decrease in the extent of interaction between PCL and clay. In the case of semi-crystalline polymers, CRR is related to the crystallinity and it can be observed from

Figure 2 that the crystallinity of the nanocomposites shows a regular decrease. This can be due to the fact that at higher loadings of Cloisite 10A, the agglomeration of Cloisite 10A hinders the chain diffusion resulting in reduced crystallinity. This can also be the reason for the observed decrease in CRR values at higher loadings of Cloisite 10A. WAXS analysis was used to calculate the crystallite size using the Scherer equation.[18] It is important to note that the addition of Cloisite 10A results in the diffusion of PCL chains into the clay galleries and thereby inducing a strain in the crystalline structure of Cloisite 10A. Figure 3(a) shows the WAXS analysis for Cloisite 10A, and the neat Cloisite 10A shows a predominant peak at 2θ of 5.02°. In the nanocomposites a very interesting phenomenon was observed, for low amounts of Cloisite 10A, (0.1 wt%) the peak at 5.2°, almost disappeared which can be due to the effective dispersion of the filler in the PCL matrix. On increasing the amount of Cloisite 10A, to 2.5 wt%, an intense peak appeared at 2.57° which showed a slight shift to 2.43° when the amount of filler was increased to 5 wt%. Similarly for nanocomposites with 2.5 and 5 wt% Cloisite 10A, a very weak peak can be observed at 4.497°. This shows that in the nanocomposites with 2.5 and 5 wt% of Cloisite 10A, there exist two different peaks, one at 2θ of 2.57° corresponding to nicely intercalated Cloisite 10A, and another weak peak at 4.497° corresponding to small amount of agglomerated Cloisite 10A, fraction. The predominant peak at lower 2θ values can be due to the effective dispersion of the Cloisite 10A, in PCL matrix, which arises due to the interaction between PCL and Cloisite 10A. While the minor peak at higher 2θ value can be due to agglomeration of Cloisite 10A. Williamson and Hall proposed that the shift in 2θ can be due to a contribution from the mean size and from inhomogeneous strain which vary quiet differently with Bragg angle.[22–24] Accordingly, to Williamson and Hall,

$$\varpi_{tot} = \varpi_s + \varpi_l \quad (1)$$

$$\varpi_s = C\varepsilon \tan\theta \quad (2)$$

While $\varpi_l = \frac{K\lambda}{l\cos\theta}$ (3)

Thus, $\varpi_{tot}\cos\theta = C\varepsilon\tan\theta + \frac{K\lambda}{l\cos\theta}$ (4)

Thereby a plot of B cosθ against sinθ should be a straight line where the slope gives the strain component while the y intercept gives the size component. Figure 3(b) shows the Willliamson-Hall plot for PCL-Cloisite 10A. The interaction between PCL and Cloisite 10A result in effective intercalation of PCL into the clay galleries resulting in considerable strain in Cloisite 10A. Now the effect of Cloisite 10A on the crystallite size was analysed in detail. The crystallite size (m) was calculated using Scherer equation[25–27],

$$m = \frac{0.9\lambda}{B\cos\theta} \quad (5)$$

Here m is the crystallite size, λ is the wavelength of the X-ray (0.154 nm), and B is the full width at half maximum (FWHM) of the peak corresponding to 2θ of 21.82°. Figure 4 shows the result obtained for neat PCL and PCL-Cloisite 10A nanocomposites. The crystallite size shows an initial increase due to the nucleating effect of Cloisite 10A and thereafter at higher loadings it show a decrease due to agglomeration. The wetting behaviour of the composites with respect to water is analysedand focused on to investigate the effect of the filler interaction with PCL matrix. Figure 5 compares the contact angle values obtained experimentally, and that theoretically expected based on the additivity rule. A large deviation from the theoretically expected contact angle values indicate extensive interaction between PCL and Cloisite 10A. Similarly at higher ladings of Cloisite 10A, PCL behaves as a super hydrophilic material which can be an advantageous factor when considering the end of the nanocomposites. Figure 6 shows the contact angle measurements for the nanocomposite with 7.5 wt% of Cloisite 10A. The contact angle values were used to calculate the wetting characteristics such as work of adhesion,[28] total surface free energy,[29] interfacial free

energy[30], spreading coefficient and Girifalco-Good's interaction parameter.[30] The change in free energy (ΔG) when a drop of liquid spreads by an infinitesimal amount is given by,

$$\Delta G = \gamma_{sl}\Delta A - \gamma_s \Delta A + \gamma_l \Delta A \cos\theta \qquad (6)$$

At equilibrium,

$$\frac{\Delta G}{\Delta A} = 0; \gamma_{sl} - \gamma_s + \gamma_l \cos\theta = 0 \qquad (7)$$

Here γ_l and $\cos\theta$ are directly measureable, while γ_{sl} and γ_s are not. According to Zisman et al.[31, 29]a plot of $\cos\theta$ against the surface tension for liquid (γ_l), can be extrapolated to give a critical surface tension, γ_{cr}, at which $\cos\theta$=1

$$\gamma_{cr} = \gamma_s \qquad (8)$$

Surface free energy, defined as the energy associated with the interface between two phases according to Owens-Wendt theory,[30,31] the total solid surface free energy is represented as

$$\gamma_s = \gamma^d_s + \gamma^p_s \qquad (9)$$

Surface energy is the energy associated with the interface between two phases. The work of adhesion, (WA) is the work required to separate the composite surface and the liquid drop

The work of adhesion, W_A, can be calculated using the equation

$$W_A = (1 + \cos\theta)\, \gamma_l \qquad (10)$$

Where γ_l is the surface tension of the liquid used for the contact angle measurement.The interfacial energy is defined as the energy necessary to form a unit area of the new interface in the system

The interfacial free energy, γ_{s1} was calculated as,

$$\gamma_{s1} = \gamma_s + \gamma_1 - W_A \qquad (11)$$

Whether a liquid will spontaneously wet and spread on the solid surface is provided by the spreading coefficient (S_c) if the value is positive whereas, a negative value of 'S_c' implies the lack of spontaneous wetting

$$S_c = \gamma_s - \gamma_{sl} - \gamma_l \quad (12)$$

Finally, the Girifalco-Good's interaction parameter quantifies the degree of interaction between the test liquid and the polymer surface. Girifalco–Goods interaction parameter (Φ), between the polymer and the liquid was determined using the equation given below,

$$\Phi = \frac{r_l(1+\cos\theta)}{2(r_l r_s)^{1/2}} \quad (13)$$

The values obtained are shown in Table 1. It can be observed from Table 1, that the work of adhesion increases as the amount of Cloisite 10A increases, followed by a decrease in the interfacial energy. The interaction parameter shows an increase as the amount of Cloisite 10A increases. All these point to effective interaction between PCL and Cloisite 10A. Figure 7 shows a schematic representation of the diffusion of PCL chains into the inter-gallery spacing of Cloisite 10A. To support this, the nature of interaction between PCL and Cloisite 10A was investigated using FTIR spectroscopy. Figure 8 shows the FTIR spectra of PCL and PCL-Cloisite 10A nanocomposites. It can be directly observed that there exist weak Vander Waal's forces of interaction between PCL and Cloisite 10A.The nature of interaction between PCL and Cloisite 10A was investigated using FTIR spectroscopy. The peak at 1724 cm^{-1} corresponding to C=O stretching showed considerable sensitivity to Cloisite 10A concentration. The intensity of the peak decreased sharply as the amount of Cloisite 10A is increased to 5 wt% indicating that the C=O group is involved in hydrogen bond formation with the organic modifier of Cloisite 10A. On increasing the Cloisite concentration to 7.5 wt%, the intensity of the peak increases indicating that the agglomeration of Cloisite 10A decreases the extent of interaction between PCL and Cloisite 10A. Optimization of the

solution parameters and operational parameters of electrospinning was done using detailed SEM analysis. This plays major role in the fibre diameter and fibre distribution. The effect of the solution concentration on the membrane morphology and the average fiber diameter were studied for four different concentrations (2, 4, 6, and 8 wt%) at an applied voltage of 15 kV. The SEM images for the composites were shown in Figure 9. For 2 and 4 wt% solution concentration, large spherical beads in combination with thin fibers were observed. Fewer beads were observed for 6 wt% solution concentration while membranes with fine fibrous structure without beads were observed for all other concentrations. Surface tension is the dominating factor in electrospinning of low concentration solutions, and membranes with many beads are usually formed in such cases. Fewer beads are observed as the polymer concentration increases, mainly due to the implied viscosity increase. Thus the polymer concentration has its own role in determining the final morphology of the electrospun nanofibers. Applied voltage can be considered as one of the main operational parameters regarding electrospinning. Here, the morphology of the membrane was examined by varying the applied voltage from 8 KV to 15 KV, by keeping the polymer concentration as 8 wt% with small amount of clay (5 wt%). In all cases, membranes with a fine fibrous structure without beads were produced. As shown in the Figure variation of the applied voltage in the range of 8 to 15 kV had no major effect on the average fiber diameter [refer Figure 10]. In addition to viscosity and applied voltage analysis of electrospun membranes of pristine polymer, we have investigated the morphological analysis of electrospun membranes of polymer nanocomposites which was prepared by the incorporation of clay platelets into the polymer matrix followed by electrospinning. In order to study the effect of the inorganic filler on the final fibrous structure, all the electrospinning processing variables were kept constant. Membranes were produced using neat and nanocomposite PCL with a clay (Cloisite 15A) content that ranged between 2.5wt% and 7.5 wt%. Solution concentration was equal to 8 wt%

and the applied voltage was 15 kV. Feed rate was maintained at 1 $ml \cdot hr^{-1}$ throughout the experiment. From Figure 11 it can be shown that, the introduction of nanofiller resulted in the formation of membranes with a more pronounced fibrous structure. Fewer beads and more uniform structures were observed as the clay content of the nanocomposite material increased to 2.5 wt% to 10 wt%. From the morphological analysis, an increase in the clay content of the electrospun nanocomposites material resulted in the production of more fine fibrous structures. This may be due to the increase in electric conductivity and viscosity of the solution caused by the addition of nanoclay. Increase in viscosity hinders the formation of droplets, resulting in the formation of fewer bead defects. The extent of dispersion of Cloisite 10A in electrospun PCL fibre was investigated using TEM analysis. Figure 12 shows the fiber distribution graph, and it can be noted that the fiber size distribution is getting narrower with the incorporation of nanoclay in to the pristine polymer solution. For pure polymer and 2.5 wt% clay solutions, the fiber diameter distribution is quite high compared to 5 wt% and 7.5 wt% clay solutions. Figure 13 shows the TEM image of PCL fibre with dispersed Cloisite 10A platelets. The Cloisite 10A layers are shown by white circles and arrows for better view and easiness of understanding. Orientation of nanoclay platelets inside the PCL nanofiber was explained through a schematic diagram (Figure 14). Here, the change in correlation length (ξ_{clay}) and the average length of the dispersed clay (L clay) layers were analyzed from the TEM images using *image j* software and is tabulated in Table 2. The correlation length of the dispersed nanoclay was found to be maximum for 2.5 wt% Cloisite 10A loading. This suggests that the nanocomposite with 2.5 wt% has maximum dispersion with partially exfoliated structure in the PCL matrix. It can be seen from the table that the correlation distance is getting decreased with the increase in clay loadings. As the clay platelets gets aligned over themselves at higher clay loadings, average length of the dispersed clay platelets were also found to be increased (Figure 14). Correlation length was found to be decreased

with the addition of Cloisite 10A, which can be attributed due to the stacking of clay platelets occurs at higher clay loadings. Figure 15 portrays the stress-strain curve for neat PCL and PCL-Cloisite 10A nanocomposites. From the Figure, it is clear that, the tensile strength of the membranes are increased with increasing filler content. Low loadings of Cloisite 10A resulted in a strong reinforcing effect, increasing the tensile modulus and inhibiting polymer drawing. Nanocomposites with 5 wt% Cloisite 10A nanofillers showed superior tensile strength compared with the neat PCL membrane. At higher clay content, the tensile behavior reverses and all the mechanical properties seemed to be retarded. This is due to the fact that clay plates have high surface energy and are easy to aggregate, which leads to the poor dispersion of them in polymer matrix. Table 3 shows the results obtained for the neat PCL and PCL-Cloisite 10A nanocomposites. Figure 16 shows the results obtained during the TG analysis of PCL and PCL-Cloisite 10A nanocomposites at different loadings of Cloisite 10A. Neat PCL shows a degradation temperature (T_d) of 320 °C, addition 5 wt% of Cloisite 10A causes a tremendous increase in T_d by around 60-80 °C. This indicates that the effective dispersion of Cloisite 10A in PCL matrix improves the thermal stability of PCL. However, 7.5 wt% addition of clay causes decrease in thermal stability due to aggregation of the clay platelets. Fibroblasts are important cell lines for wound healing and skin regeneration. PCL-Cloisite 10A nanocomposite, with 5 wt% of nanofiller was selected for cell viability studies owing to their improved thermal, mechanical properties and super hydrophilic characteristics and the growth of fibroblast cells was evaluated using MTT assay. Optical observation using phase contrast microscope was also done in order to follow the cytocompatibility of the porous nanocomposite scaffolds. It can be seen from Figure 17, that viability of fibroblast cells were found to be dose dependent; Number of viable cells were decreasing in higher concentrations. Cells showed much better viability (96%) when the concentration of *an chitinase* was 1 µl as compared with higher concentrations of *an chitinases* (5, 10, 20 µL). It

can also be observed that, when the concentration of *anchitinase* was more than 10 µl, the cell viability decreased drastically, indicating the presence of non-living cells. The results here demonstrated that an appropriate concentration of *anchitinase* as well as *afchitinase* would be beneficial for improving cytocompatibility of porous nanocomposite scaffolds. *Anchitinase* having the concentration of 1 µl showed the lowest cytotoxicity, which is important for wound healing and skin regeneration. The morphology of L929 fibroblast cells cultured on different concentration of *anchitinase* as well as *afchitinase* was further observed by a phase contrast microscope and the results were shown in Figure 14. It could be seen clearly that the fibroblast cells were homogeneously distributed on all the samples. After 24 hours of cell culture, the cells on all samples mainly showed a characteristic morphology change as we shift from *anchitinase* concentration of 1µL to 20 µL. Thus, it is clearly evident that PCL-Cloisite 10A (5 wt%) electrospun nanocomposite scaffolds could promote fibroblast cells growth. In our study, *anchitinase* as well as *afchitinase* concentration of 1 µl was found to be more appropriate to promote the attachment and growth of fibroblast cells.

Conclusions

Fibrous PCL-Cloisite 10A nanocomposites fabricated by electrospinning was subjected to detailed investigation to study the effect of addition of an interacting filler on the segmental dynamics, morphology and thermal properties of PCL. In all cases, the addition of the Cloisite 10A resulted in the formation of more fine fibers with fewer bead defects and in narrower fiber size distributions which can be attributed to the increase in solution's electric conductivity and viscosity caused by the addition of nanoclay. Strong hydrogen bonding interaction between PCL and Cloisite 10A plays a vital role in the segmental dynamics morphology and thermal properties of PCL. Diffusion of PCL chains into the inter gallery spacing of Cloisite 10A is evidenced by the WAXS analysis. Thus the addition of Cloisite

10A in PCL has a dramatic influence on the crystalline regions of the host (PCL) and guest (Cloisite 10A). A sharp decrease in the water contact angle of PCL further proves the interaction between PCL and Cloisite 10A. Detailed investigation of the nature of relation between PCL and Cloisite 10A shows the existence of strong hydrogen bonding interaction. Similarly the addition of Cloisite 10A has a significant improvement in thermals stability of PCL. The interaction between PCL and Cloisite 10A plays a major role in improving the tensile strength and modulus of the nanocomposites. This interaction can be the reason for the improvement in mechanical properties, segmental mobility, mechanical properties and biocompatibility of PCL-Cloisite 10A nanocomposites when the other nanocomposites produced conflicting results. The increase in hydrophilic nature of the composites with the addition of Cloisite 10A is a strong indication to use PCL-Cloisite 10A system as a good alternative in tissue engineering applications as it can promote cell adhesion and proliferation.

Acknowledgement:

The authors are thankful to the Department of Biotechnology and DST Nanomission, Government of India, for the financial support.

References

1 Z.-M. Huang, Y.-Z. Zhang, M. Kotaki and S. Ramakrishna, *Compos. Sci. Technol.*, 2003, **63**, 2223–2253.
2 N. Bhardwaj and S. C. Kundu, *Biotechnol. Adv.*, 2010, **28**, 325–347.
3 G. C. Rutledge and S. V. Fridrikh, *Adv. Drug Deliv. Rev.*, 2007, **59**, 1384–1391.
4 Z. Chen, X. Mo and F. Qing, *Mater. Lett.*, 2007, **61**, 3490–3494.
5 K. M. Manesh, P. Santhosh, A. Gopalan and K.-P. Lee, *Anal. Biochem.*, 2007, **360**, 189–195.
6 N. Ristolainen, P. Heikkilä, A. Harlin and J. Seppälä, *Macromol. Mater. Eng.*, 2006, **291**, 114–122.
7 L. Li, L. M. Bellan, H. G. Craighead and M. W. Frey, *Polymer*, 2006, **47**, 6208–6217.
8 T. K. Pham, P. K. Chong, C. S. Gan and P. C. Wright, *J. Proteome Res.*, 2006, **5**, 3411–3419.
9 R. W. Tuttle, A. Chowdury, E. T. Bender, R. D. Ramsier, J. L. Rapp and M. P. Espe, *Appl. Surf. Sci.*, 2008, **254**, 4925–4929.
10 Y. H. Lee, J. H. Lee, I.-G. An, C. Kim, D. S. Lee, Y. K. Lee and J.-D. Nam, *Biomaterials*, 2005, **26**, 3165–3172.

11 J. H. Hong, E. H. Jeong, H. S. Lee, D. H. Baik, S. W. Seo and J. H. Youk, *J. Polym. Sci. Part B Polym. Phys.*, 2005, **43**, 3171–3177.
12 D. Ratna, S. Divekar, S. Patchaiappan, A. B. Samui and B. C. Chakraborty, *Polym. Int.*, 2007, **56**, 900–904.
13 E. T. Arung, K. Yoshikawa, K. Shimizu and R. Kondo, *Fitoterapia*, 2010, **81**, 120–123.
14 E. T. Arung, K. Shimizu and R. Kondo, *Biol. Pharm. Bull.*, 2006, **29**, 1966–1969.
15 E. T. Arung, B. D. Wicaksono, Y. A. Handoko, I. W. Kusuma, D. Yulia and F. Sandra, *Trop. J. Pharm. Res.*, 2009, **8**.
16 G. Adam and J. H. Gibbs, *J. Chem. Phys.*, 1965, **43**, 139–146.
17 J. D. Stevenson, J. Schmalian and P. G. Wolynes, *Nat. Phys.*, 2006, **2**, 268–274.
18 A. Bharati, P. Xavier, G. P. Kar, G. Madras and S. Bose, *J. Phys. Chem. B*, 2014, **118**, 2214–2225.
19 A. Saiter, J. M. Saiter and J. Grenet, *Eur. Polym. J.*, 2006, **42**, 213–219.
20 Y. Nie, X. Ye, Z. Zhou, T. Hao, W. Yang and H. Lu, *RSC Adv.*, 2015, **5**, 17726–17731.
21 G. W. Beall and C. E. Powell, *Fundamentals of Polymer-Clay Nanocomposites*, Cambridge University Press, 2011.
22 A. Llordés, A. Palau, J. Gázquez, M. Coll, R. Vlad, A. Pomar, J. Arbiol, R. Guzmán, S. Ye, V. Rouco, F. Sandiumenge, S. Ricart, T. Puig, M. Varela, D. Chateigner, J. Vanacken, J. Gutiérrez, V. Moshchalkov, G. Deutscher, C. Magen and X. Obradors, *Nat. Mater.*, 2012, **11**, 329–336.
23 M. E. A. A. K. Zak, *Solid State Sci.*, 2013, **13**.
24 P. Bindu and S. Thomas, *J. Theor. Appl. Phys.*, 2014, **8**, 123–134.
25 S. Chandran, F. Antolasic, K. J. Eichhorn, R. A. Shanks and S. Thomas, *RSC Adv.*, 2014, **4**, 25420–25429.
26 A. L. Patterson, *Phys. Rev.*, 1939, **56**, 978–982.
27 U. Holzwarth and N. Gibson, *Nat. Nanotechnol.*, 2011, **6**, 534–534.
28 Y. Xiu, L. Zhu, D. W. Hess and C. P. Wong, *J. Phys. Chem. C*, 2008, **112**, 11403–11407.
29 P. Becher, *J. Colloid Interface Sci.*, 1977, **59**, 429–432.
30 F. Fenouillot, P. Cassagnau and J.-C. Majesté, *Polymer*, 2009, **50**, 1333–1350.
31 R. J. Good and L. A. Girifalco, *J. Phys. Chem.*, 1960, **64**, 561–565.
32 S. Wang, Y. Zhang, N. Abidi and L. Cabrales, *Langmuir*, 2009, **25**, 11078–11081.
33 V. Gurau, M. J. Bluemle, E. S. De Castro, Y.-M. Tsou, J. A. Mann Jr. and T. A. Zawodzinski Jr., *J. Power Sources*, 2006, **160**, 1156–1162.
34 S. Nuriel, L. Liu, A. H. Barber and H. D. Wagner, *Chem. Phys. Lett.*, 2005, **404**, 263–266.

Table 1: The contact angle values for PCL and PCL- Cloisite 10A nanocomposites

Sample	Contact angle (°)	Work of adhesion $W_A = (1 + \cos\theta)\gamma_l$ mJ/m^2	Interfacial energy $\gamma_{sl} = \gamma_s + \gamma_l - W_A$ mJ/m^2	Spreading coefficient $S_c = \gamma_s - \gamma_{sl} - \gamma_l$ mJ/m^2	Interaction parameter $\Phi=[(1+\cos\theta)\gamma_l]/2(\gamma_s\gamma_l)^{1/2}$
PCL	94.15	66.93	43.81	-78.67	0.9232
2.5 wt% Cloisite 10A	89.55	75.56	33.44	-75.04	0.9344
5wt% Cloisite 10A	79.19	82.48	26.48	-58.12	0.9389
7.5 wt% Cloisite 10A	74.03	88.66	20.85	-52.94	0.9402

Table 2: Average length and Correlation length of Cloisite 10A in PCL-Cloisite 10A nanocomposites

	2.5 wt%	5 wt%	7.5 wt%
L Cloisite 10A (nm)	78 ± 16	215 ± 21	278 ± 32
ξ Cloisite 10A (nm)	85 ± 03	35 ± 04	27 ± 07
d spacing (Å)(XRD)	42.68	41.22	40.65

Table 3: Results obtained for neat PCL and PCL-Cloisite 10A nanocomposites

Sample details	Ultimate (MPa)	Elongation at break (%)	Tensile modulus (MPa)	Yield stress (MPa)	Youngs Modulus(MPa)
Neat PCL	1.63	192.9	1.27	0.96	2.6
2.5 wt%	1.93	173.6	1.49	1.58	3.0

5 wt%	1.90	178.1	1.63	1.89	4.4
7.5 wt%	1.61	148.2	1.58	1.01	1.9
10 wt%	1.38	137.4	1.57	1.37	1.8

Figure 1: *Structural details of Cloisite 10A with the modifier shown by red lines*

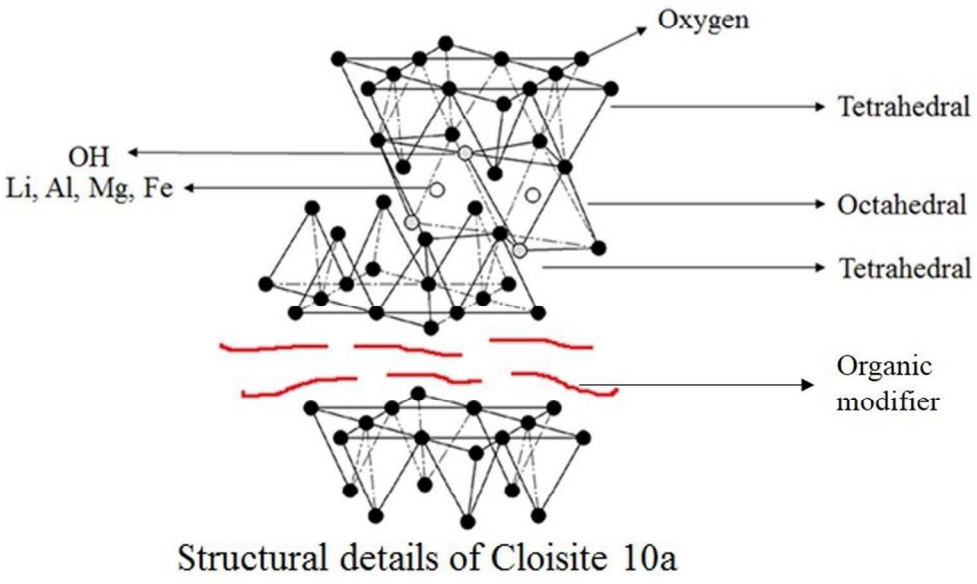

164x107mm (150 x 150 DPI)

Figure 2: *CRR and normalized crystallinity for PCL and PCL-closite 10A nanocomposites as a function of the amount of closite 10A and the corresponding optical microscopy images, where (a) represents neat PCL and (b) nanocomposite with 5 wt% clay*

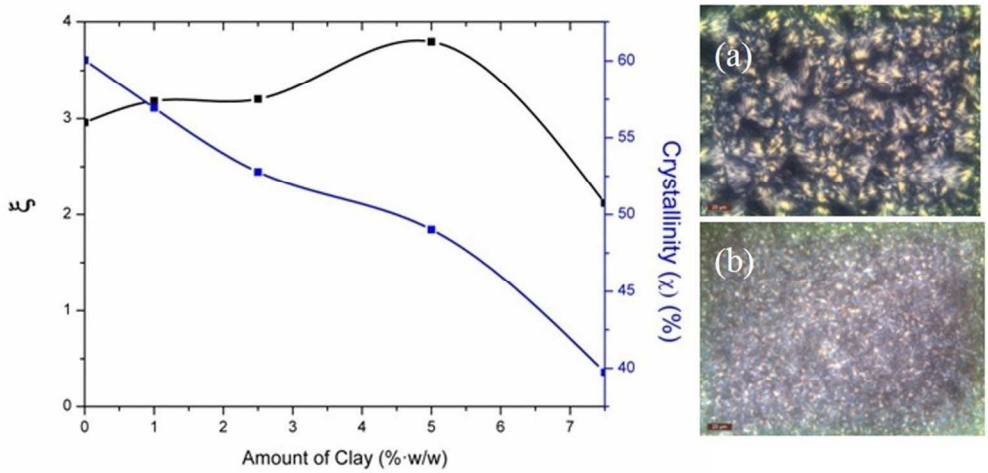

185x110mm (150 x 150 DPI)

Figure 3: (a) WAXS analysis for Cloisite 10A, and nanocomposites, (b) Williamson-Hall fitting for the Cloisite 10A

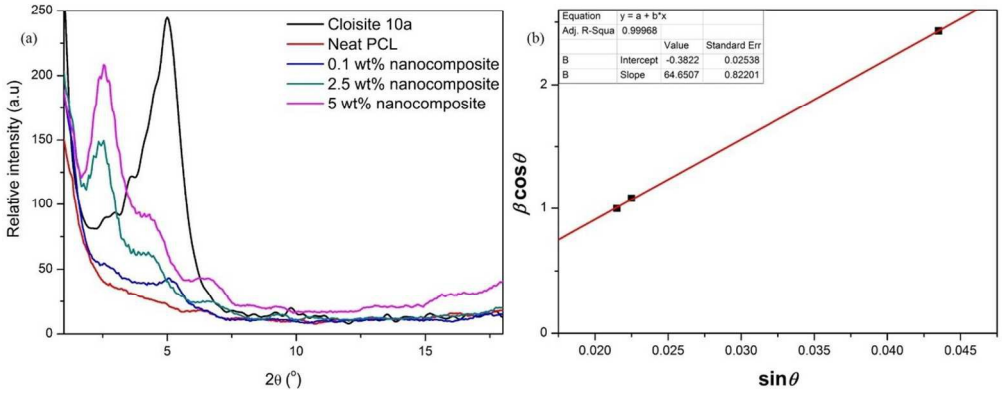

248x117mm (150 x 150 DPI)

Figure 4: *Crystallite size (m) as a function of the amount of Cloisite 10A*

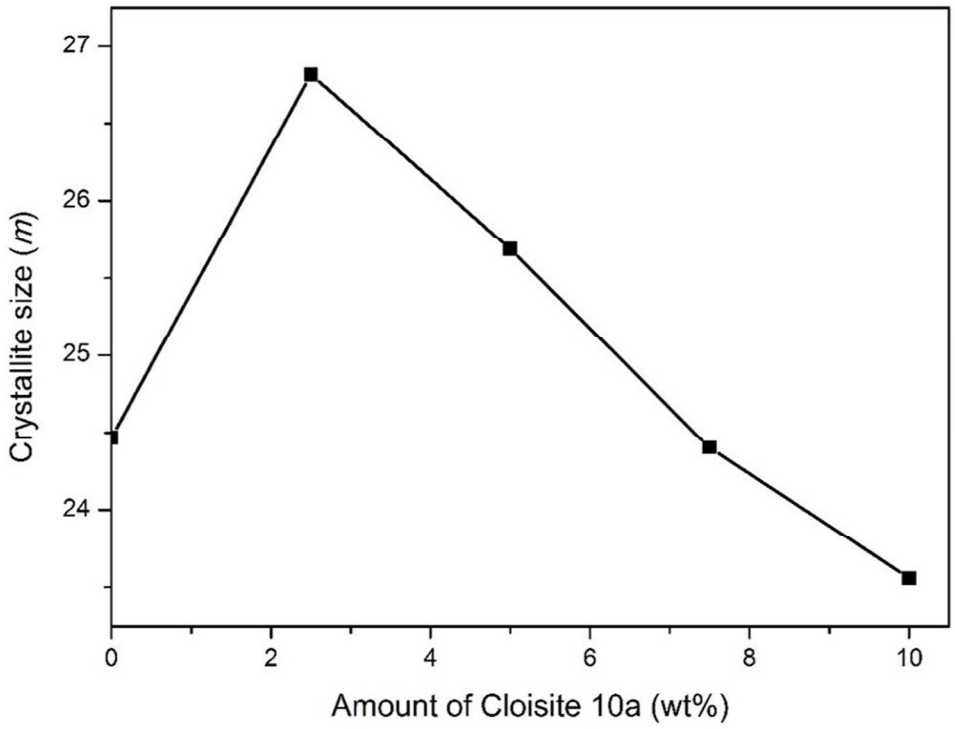

168x134mm (150 x 150 DPI)

Figure 5: *Theoretically expected and experimentally observed contact angle values for PCL-Cloisite 10A nanocomposites*

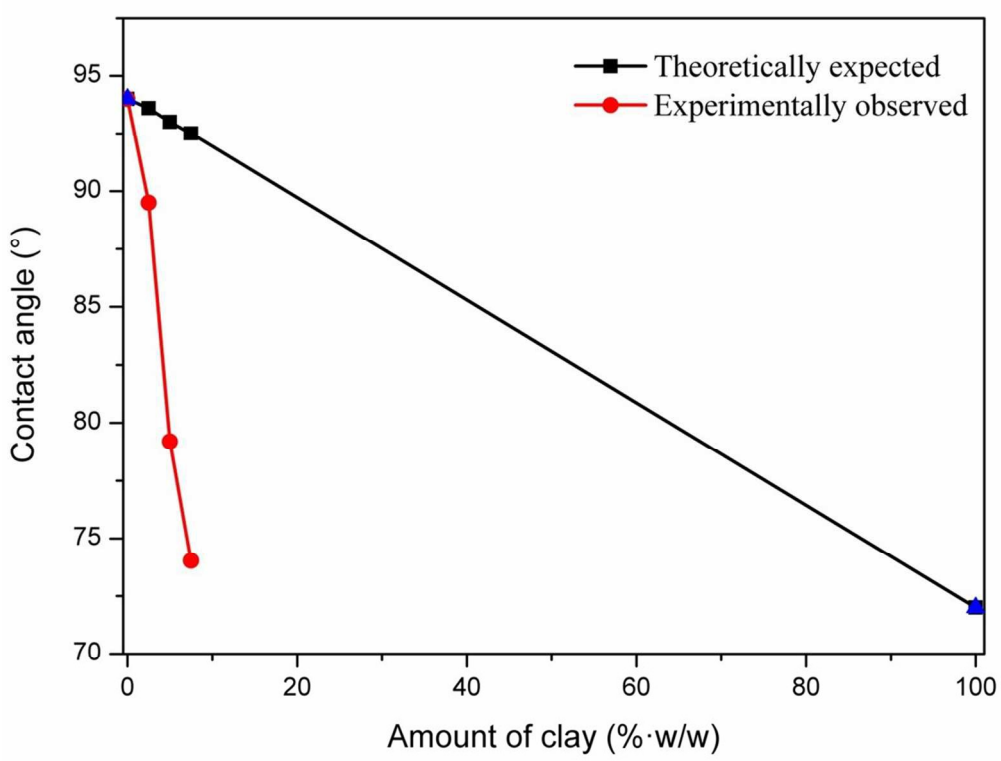

200x166mm (150 x 150 DPI)

Figure 6: Contact angle measurements of PCL-Cloisite 10A nanocomposites (7.5 wt%) with respect to time; (a) at the start of experiment (b) after 10 minutes (c) after 20 minutes (d) after 22 minutes

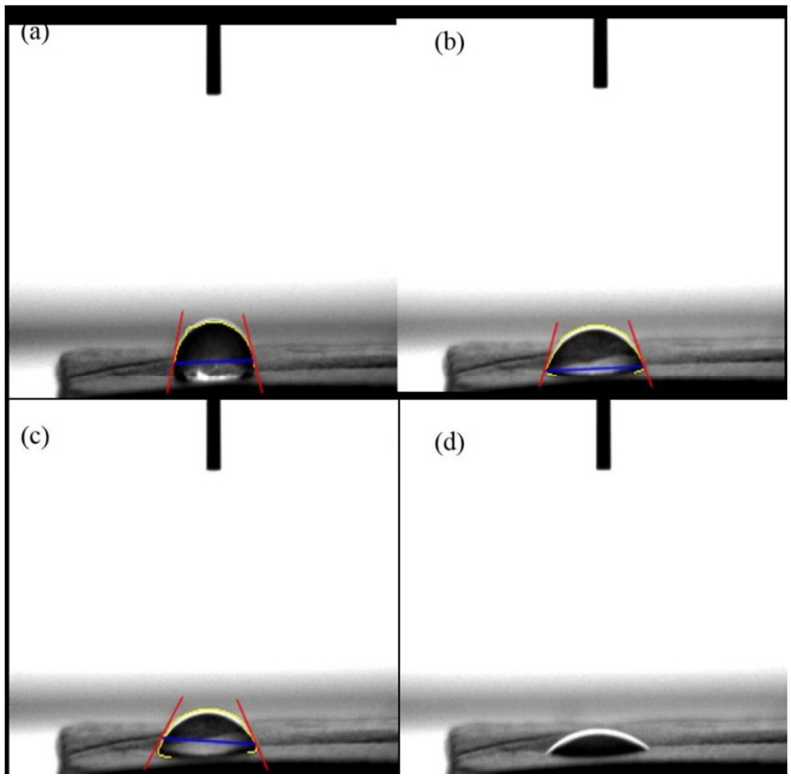

169x151mm (150 x 150 DPI)

Figure 7: *Schematic representation of the interaction/ diffusion of PCL chains with Cloisite 10A*

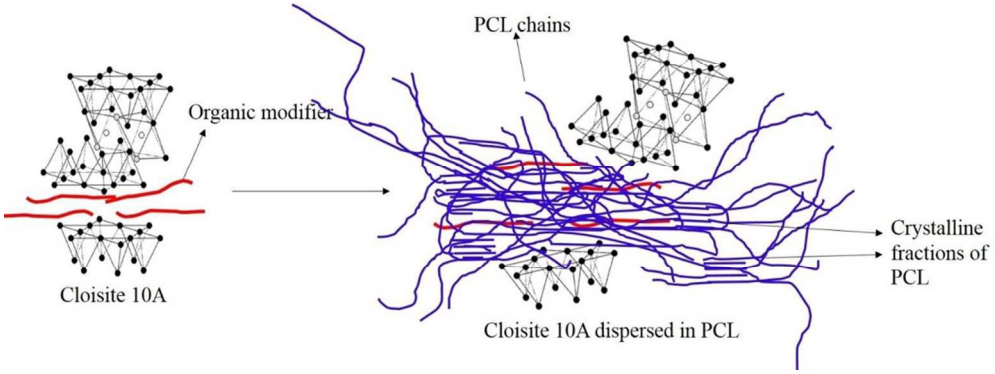

201x81mm (150 x 150 DPI)

Figure 8: *FTIR spectra of PCL and PCL-Cloisite 10A nanocomposites*

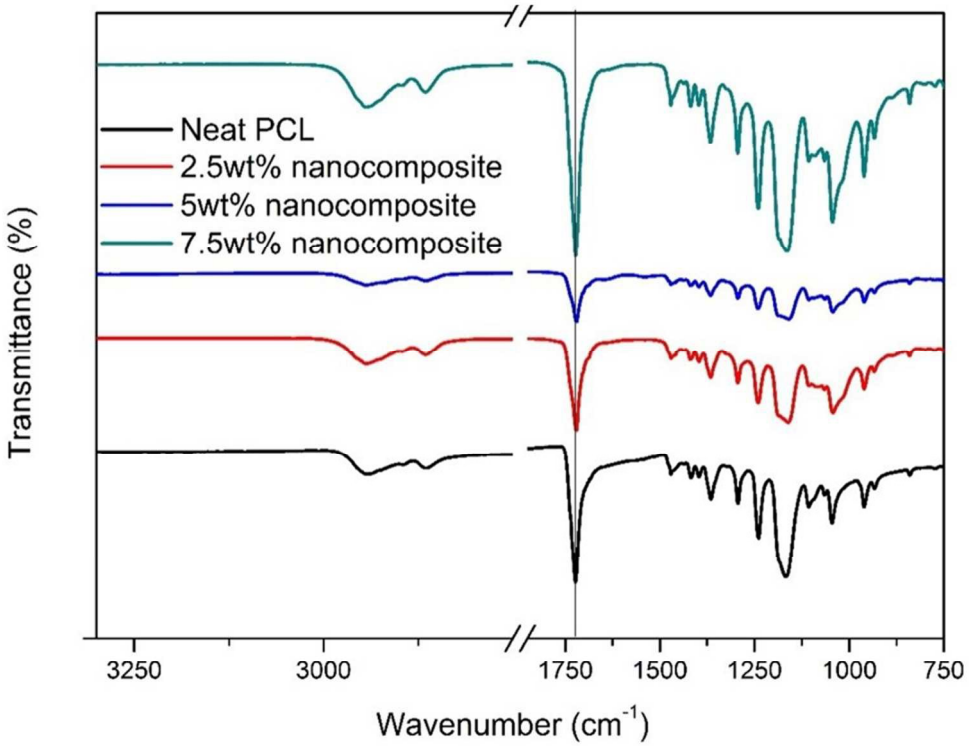

169x139mm (150 x 150 DPI)

Figure 9: *SEM images of electrospun neat PCL membrane having different solution concentrations a) 2 wt.% b) 4 wt.% and c) 6 wt.%*

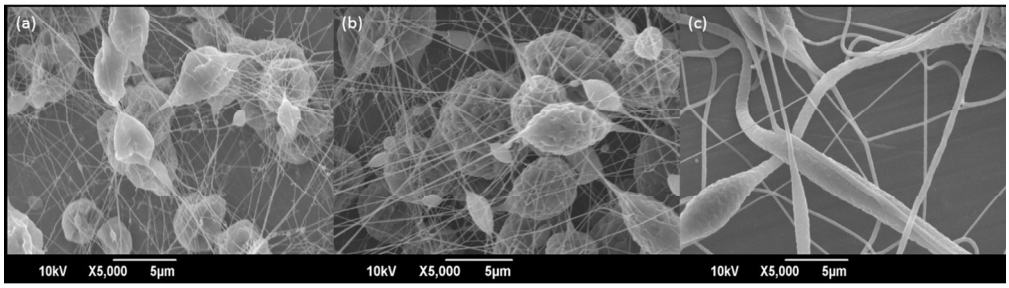

257x89mm (150 x 150 DPI)

Figure 10: *SEM images of electrospun neat PCL membrane at different applied potentials (a) 8 kV and (b) 15 kV*

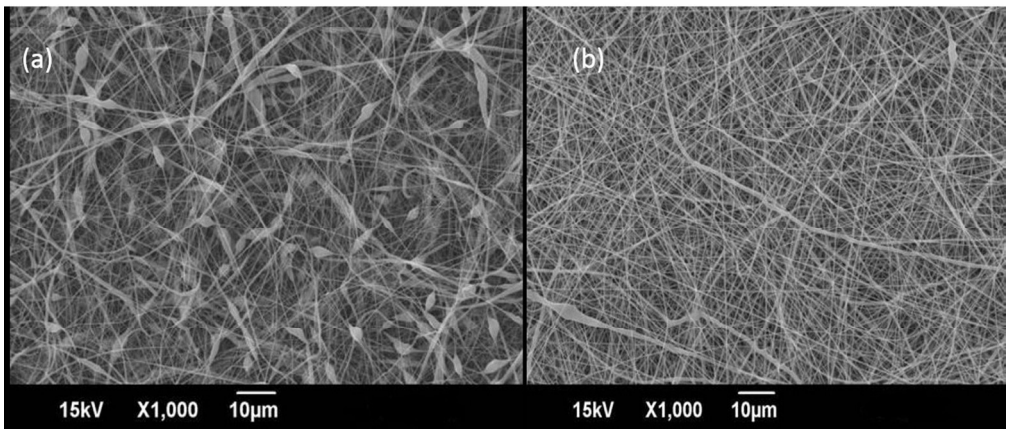

219x109mm (150 x 150 DPI)

Figure 11: *SEM images of electrospun neat PCL membranes and nanocomposite membranes: (a) neat PCL (b) 2.5 wt% nanocomposite (c) 5 wt% nanocomposite (c) 7.5 wt% nanocomposite*

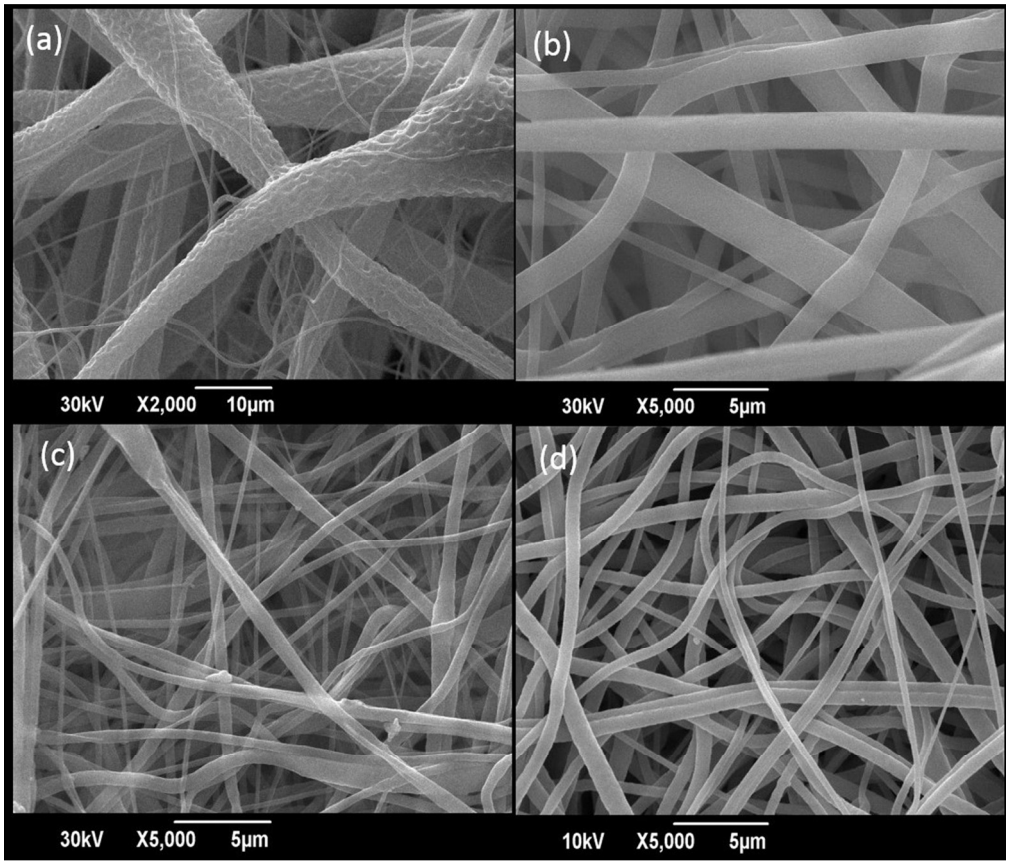

181x174mm (150 x 150 DPI)

Figure 12: Fiber diameter distribution of electrospun PCL membranes. (a) Neat PCL (b) 2.5 wt%, (c) 5 wt% nanocomposites

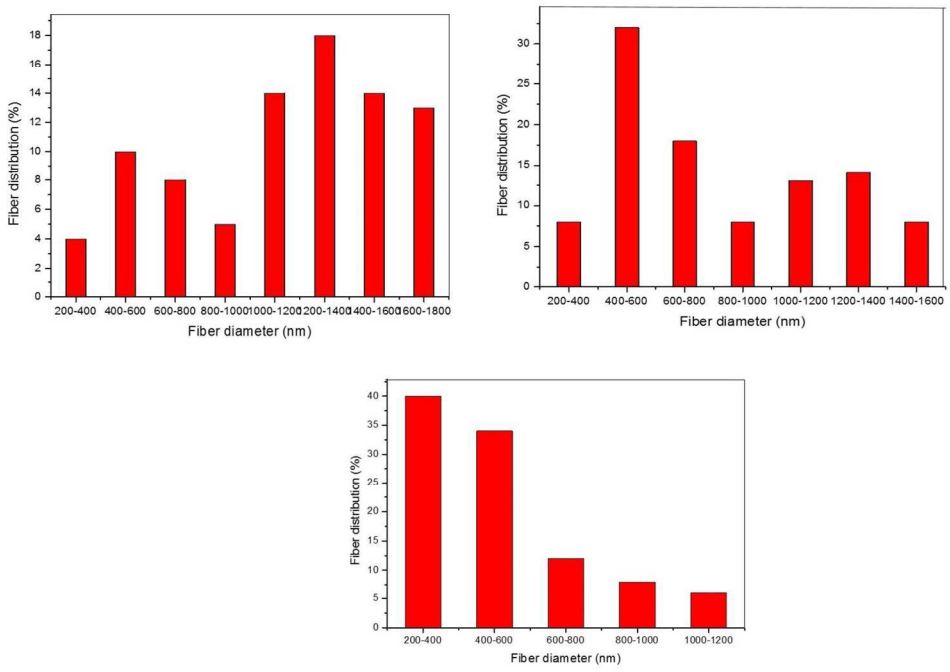

266x194mm (150 x 150 DPI)

Figure 13: *TEM image of electrospun PCL fibre with Cloisite 10A platelets (for the nanocomposite with (a) 2.5 wt%, (b)5wt% of Cloisite 10A*

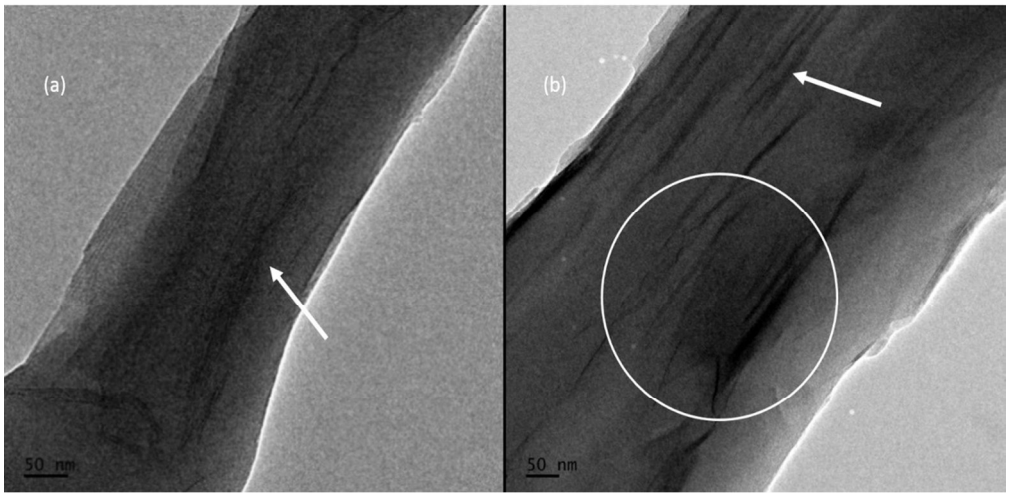

219x123mm (150 x 150 DPI)

Figure 14: *Schematic representation of orientation of clay platelets along PCL nanofiber at a) lower clay loading (2.5 wt%) and b) higher clay loading (7.5 wt%)*

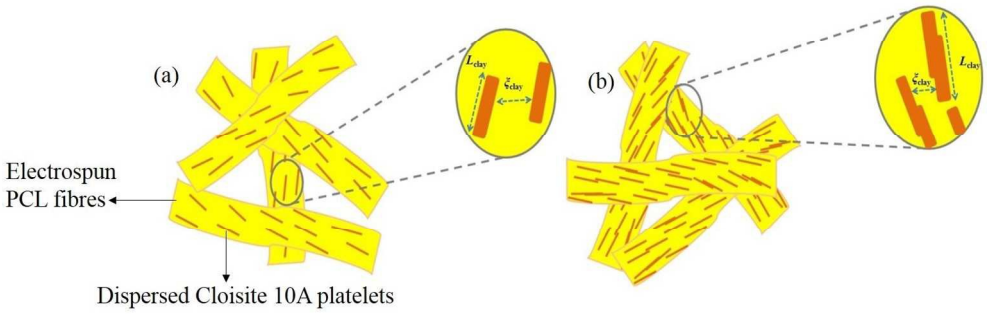

275x103mm (150 x 150 DPI)

Figure 15: *Stress- strain curves of neat PCL and PCL Cloisite 10A nanocomposite membranes*

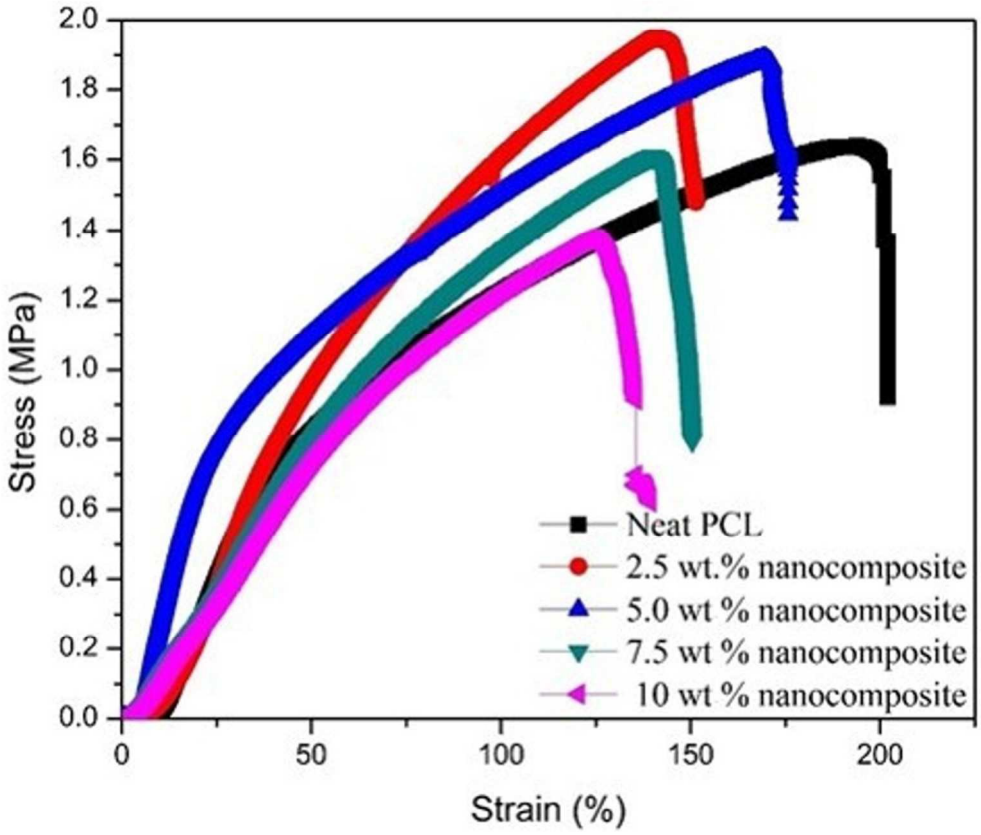

172x156mm (150 x 150 DPI)

Figure 16: *TG curves for PCL and PCL-Cloisite 10A nanocomposites*

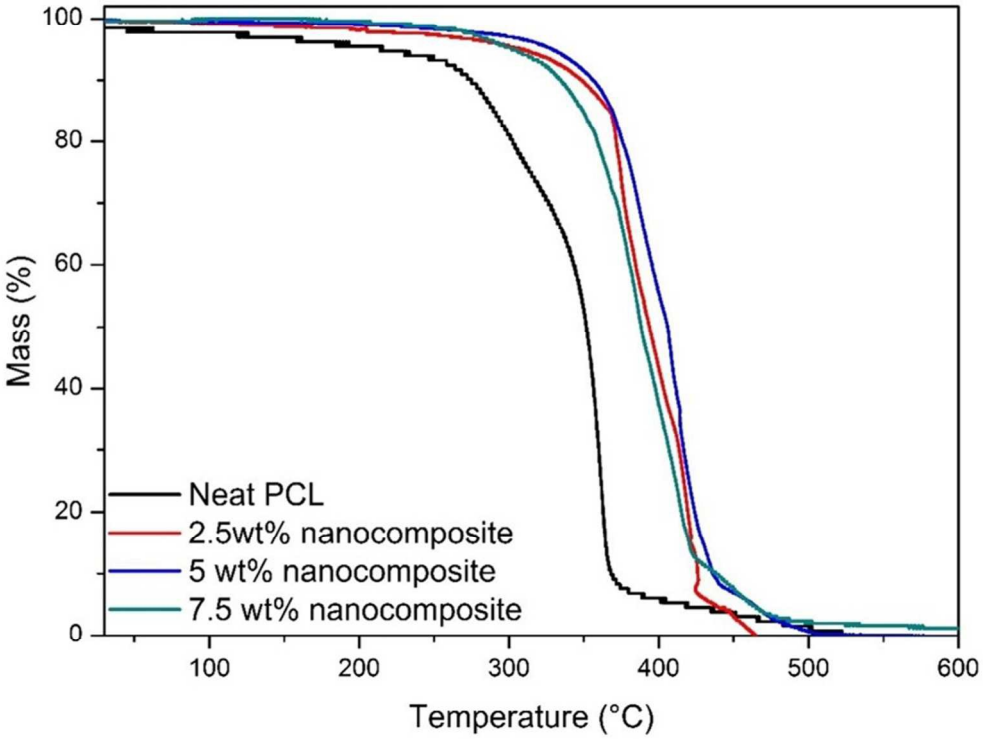

157x129mm (150 x 150 DPI)

Figure 17: *Viability and proliferation of L929 fibroblast cells after culture for 24 hrs evaluated by MTT assay. a) Control cells b) Anchitinase 1 μL c) An chitinase 10 μL d) Afchitinase 1 μL e) An chitinase 10 μL for PCL-Cloisite 10A nanocomposites with 5 wt% of Cloisite 10A*

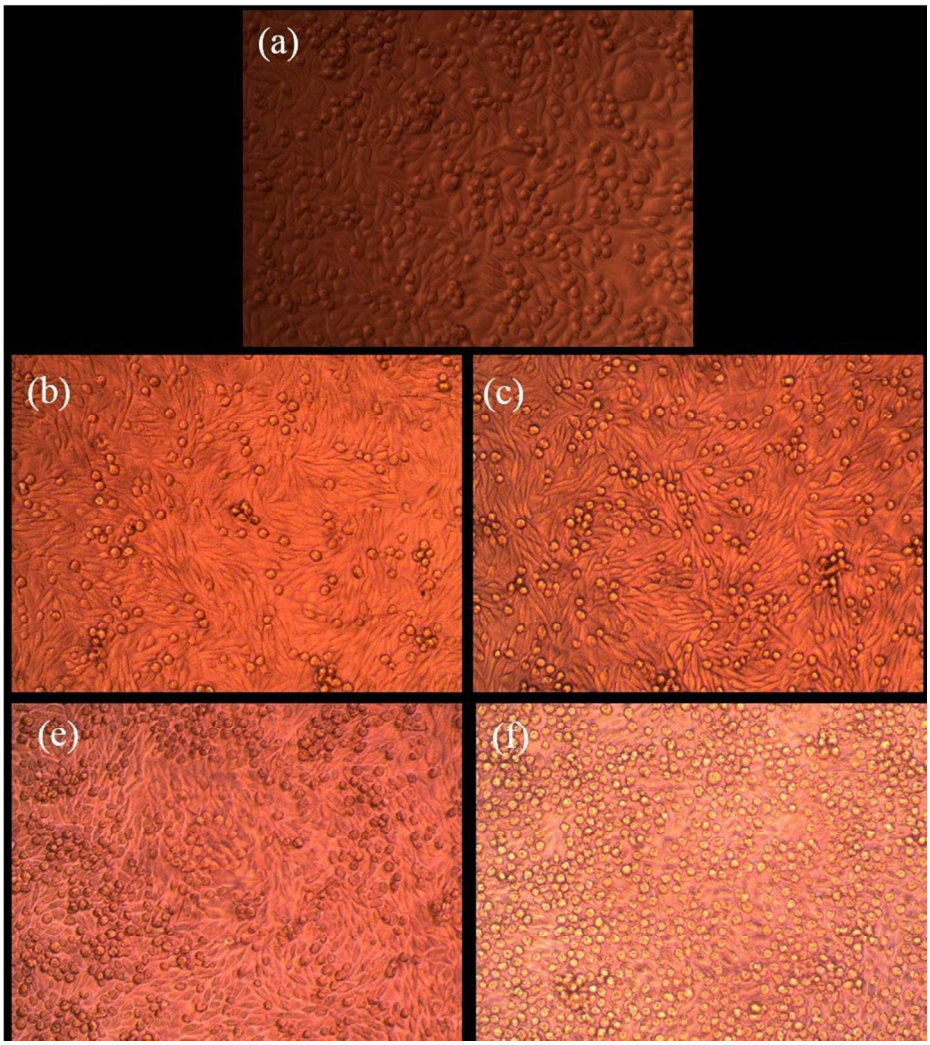

169x194mm (150 x 150 DPI)

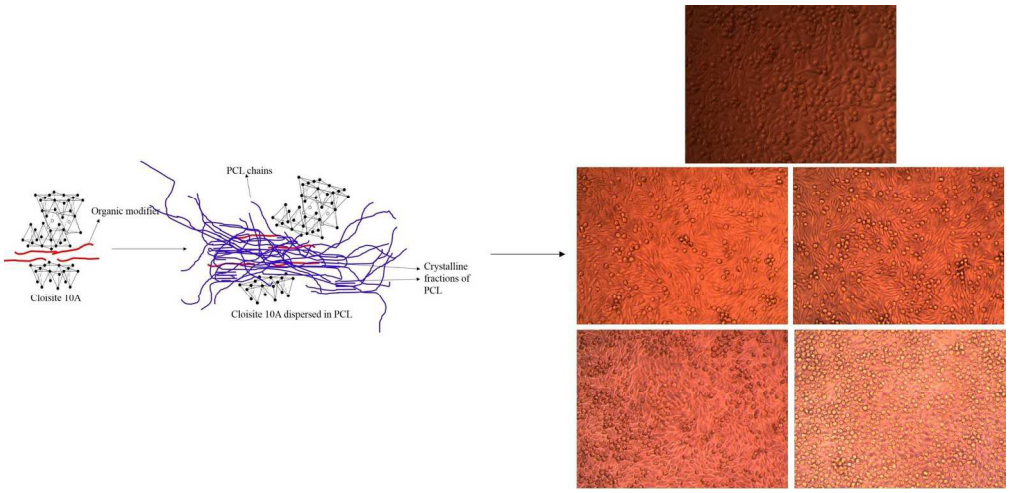

361x174mm (150 x 150 DPI)